Electronic Supplementary Information

An ultramicroporous multi-walled metal–organic framework for efficient C_2H_2/CO_2 separation under humid conditions

Weize Wang,[a] Wenke Yuan,[a] Cunding Kong,[b] Yuchen Yang,[a] Shuting Xi,[c] Xiangyu Liu,*[b] and Bo Liu*[a]

[a]College of Chemistry & Pharmacy, Northwest A&F University, Yangling 712100, P. R. China. E-mail: chemliubo@nwsuaf.edu.cn

[b]State Key Laboratory of High-efficiency Utilization of Coal and Green Chemical Engineering, College of Chemistry and Chemical Engineering, Ningxia University, Yinchuan 750021, P. R. China. E-mail: xiangyuliu432@126.com

[c]Analysis and Testing Center, Ningxia University, Yinchuan 750021, P. R. China

Contents

Experimental section

Materials and general methods

All chemicals were purchased from commercial suppliers and used as received without further purification. Powder X-ray diffraction (PXRD) data were recorded on a Bruker D8 ADVANCE X-ray powder diffractometer (Cu Kα, λ = 1.5418 Å). Thermogravimetric analysis (TGA) was carried out in a nitrogen stream using a Netzsch TG209F3 equipment at a heating rate of 10 °C min^{-1}. Fourier transform infrared spectroscopy (FT-IR) measurement was performed on a Nicolet Avatar 360 FT-IR. C, N and H contents were determined by a PerkinElmer 2400C Elemental Analyzer.

Adsorption measurements

The as-synthesized In-TATB was activated by heating at 433 K for 8 h under a dynamic vacuum. Adsorption measurements were performed on a Micrometrics ASAP 2020 Plus adsorption analyzer. Kinetic adsorption measurements and water vapor adsorption isotherms were conducted by the Intelligent Gravimetric Analyzer (BSD-DVS, CN), which uses a gravimetric technique to accurately measure the gas adsorption and desorption on materials under constant temperature (298 K) and pressure (1 bar) conditions.

GCMC simulation methodology

Grand Canonical Monte Carlo (GCMC) simulations were performed using Materials Studio package. The 2×2×2 supercell was used for the simulations. The partial charges for atoms of the framework were derived from QEq method.[1] All the parameters for atoms of In-TATB were modeled with the CompassIII forcefield.[2] The LJ potential parameters for C_2H_2 and CO_2 were taken from the Optimized Potentials for Liquid Simulations–All Atom (OPLS-AA) and TraPPE force field, respectively.[3,4] A cutoff distance of 7.5 Å was used for LJ interactions, and the Coulombic interactions were calculated by using Ewald summation. For each run, the 5×10^6 equilibration steps, 5×10^6 production steps were employed.

Structure of In-TATB was optimized in the Dmol3 module, using the generalized gradient approximation (GGA) with the Perdew-Burke-Ernzerhof (PBE) functional and the double numerical plus d-functions (DNP) basis set. The optimized structures are in great consistency with the experimentally determined crystal structures. The electron density data obtained from these calculations were used to construct the 0.15 e^{-} $Å^{-3}$ electron density isosurfaces, with a grid interval of 0.1 Å. The force and energy convergence criterion were set to 0.002 Ha $Å^{-1}$ and 10^{-5} Ha, respectively.

The binding energy (ΔE) was calculated as

$$\Delta E \text{ (eV)} = 27.212 \times (E_{total}(\text{Ha}) - E_1(\text{Ha}) - E_2(\text{Ha}))$$

where the E_{total} is the energy of the optimized system; E_1 is the energy of the In-TATB; E_2 is the energy of C_2H_2 or CO_2.

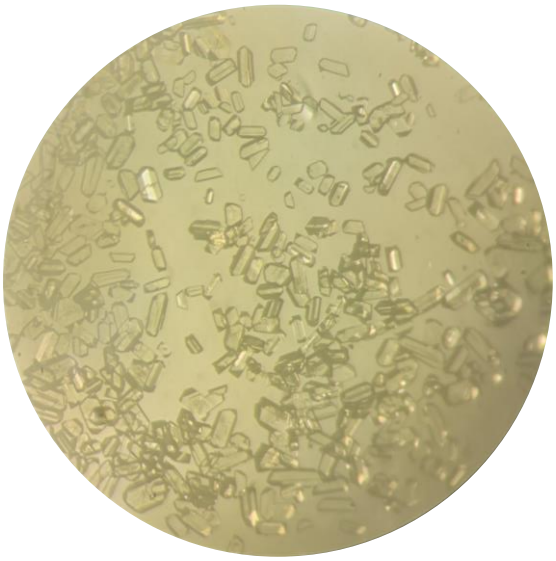

Fig. S1 Photograph of the crystal under the microscope.

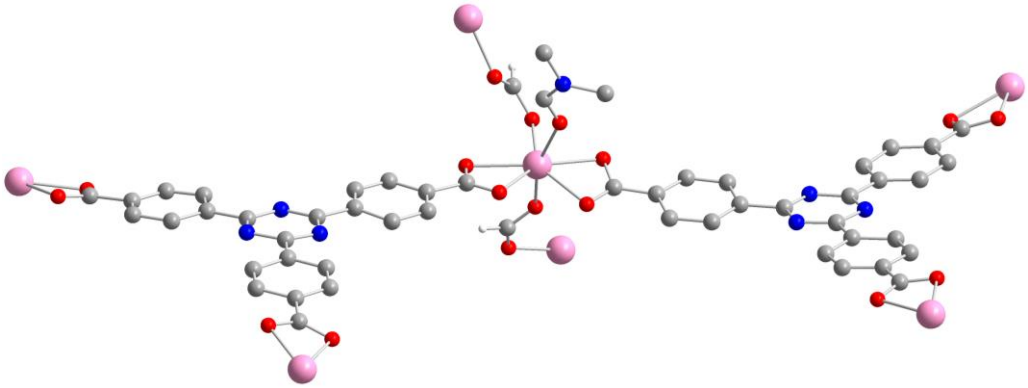

Fig. S2 The coordination environment of In^{3+} ions in In-TATB.

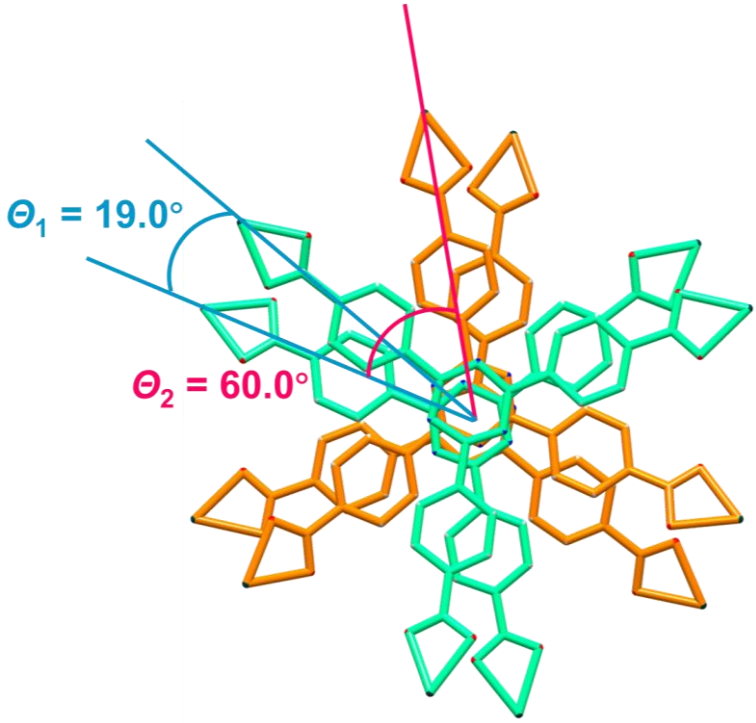

Fig. S3 The rotational angle (θ_1) and deflection angle (θ_2) between the two $TATB^{3-}$ molecules.

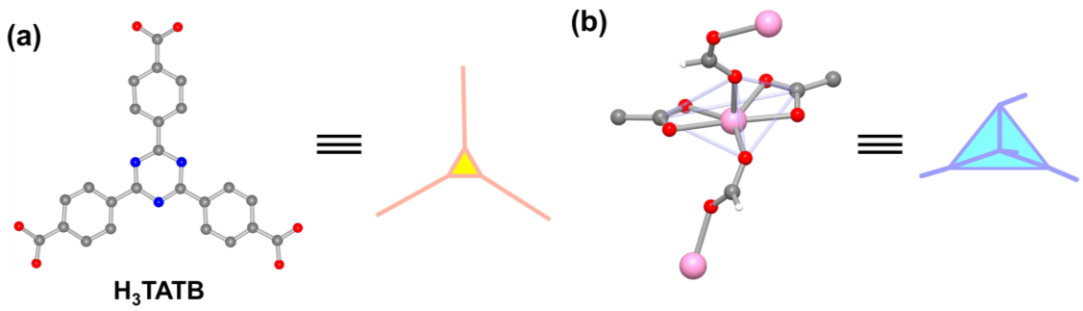

Fig. S4 Deconstruction of In-TATB for topological analysis: (a) Simplification of the $TATB^{3-}$ molecule into a yellow triangle. (b) Simplification of the In^{3+} ion into a light blue tetrahedron.

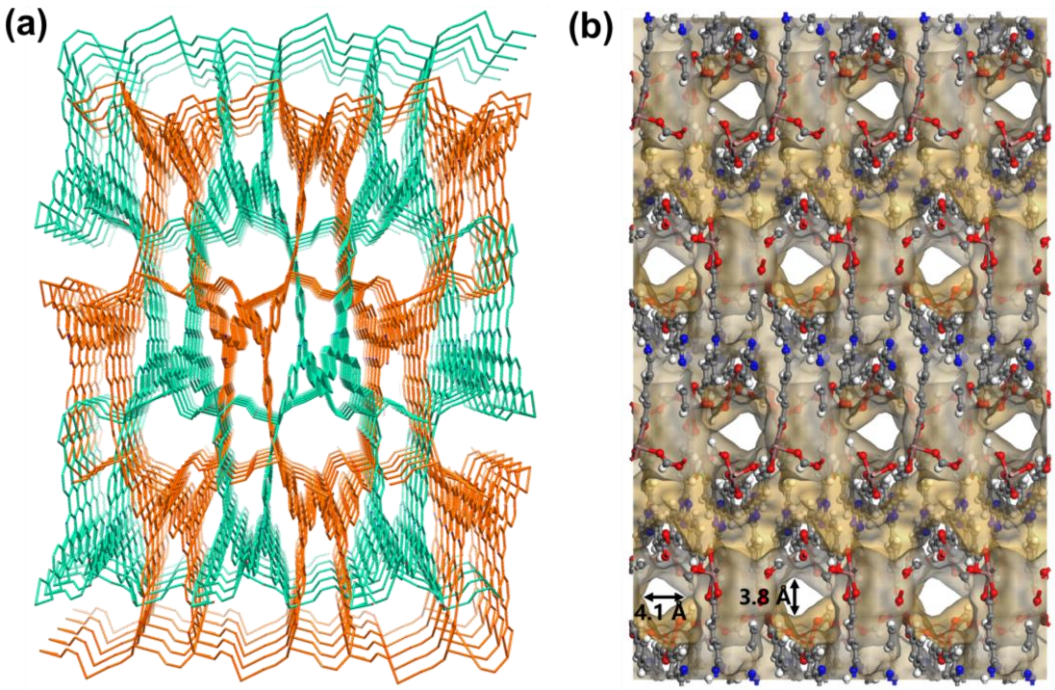

Fig. S5 (a) Porous window and (b) Connolly surface representation of In-TATB along the *b* axis.

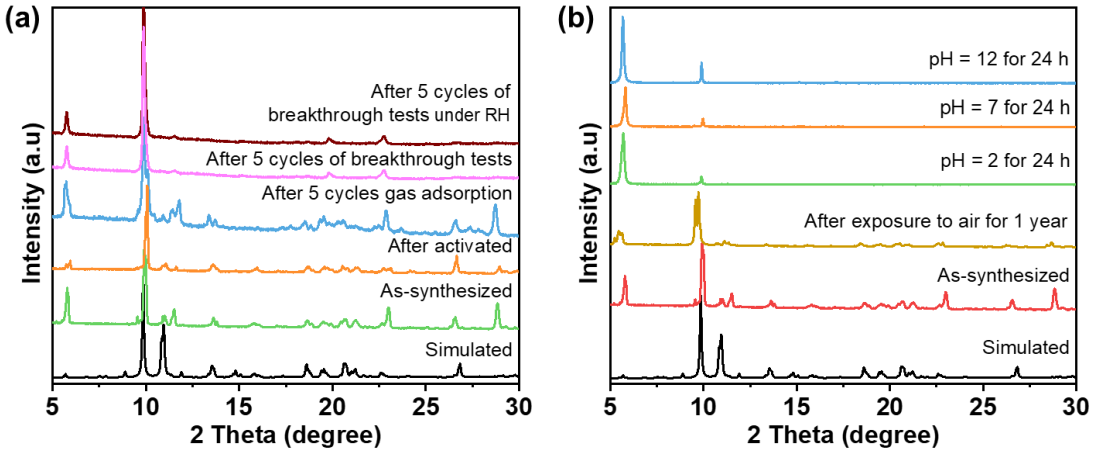

Fig. S6 PXRD patterns of In-TATB were obtained under different treated conditions.

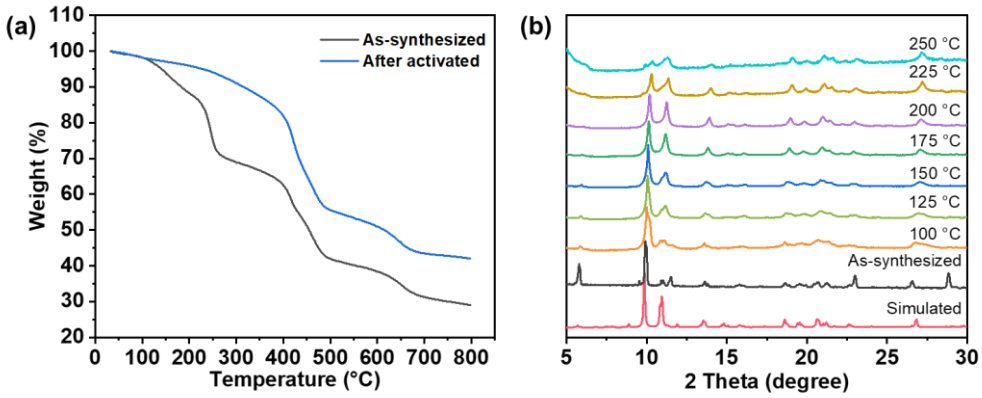

Fig. S7 (a) TGA curves and (b) variable-temperature PXRD patterns of In-TATB.

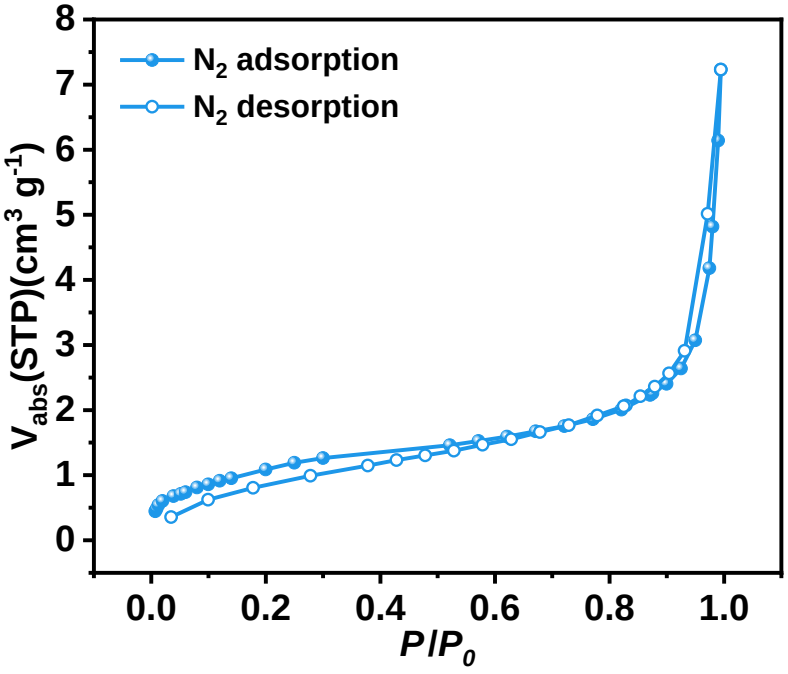

Fig. S8 N_2 adsorption isotherm of In-TATB at 77 K.

Calculation of IAST adsorption selectivity

The experimental isotherm data for pure CO_2 and C_2H_2 (measured at 298 K) were fitted using a single-site Langmuir–Freundlich (L–F) model:

$$q = \frac{a_1 * b_1 * P^{c_1}}{1 + b_1 * P^{c_1}}$$

Where q and p are adsorbed amounts and pressures of component i, respectively.

The adsorption selectivity for binary mixtures of C_2H_2/CO_2 is defined by

$$S_{i/j} = \frac{x_i * y_j}{x_j * y_i}$$

were calculated using the Ideal Adsorption Solution Theory (IAST) of Myers and Prausnitz.

Where x_i is the mole fraction of component i in the adsorbed phase and y_i is the mole fraction of component i in the bulk.

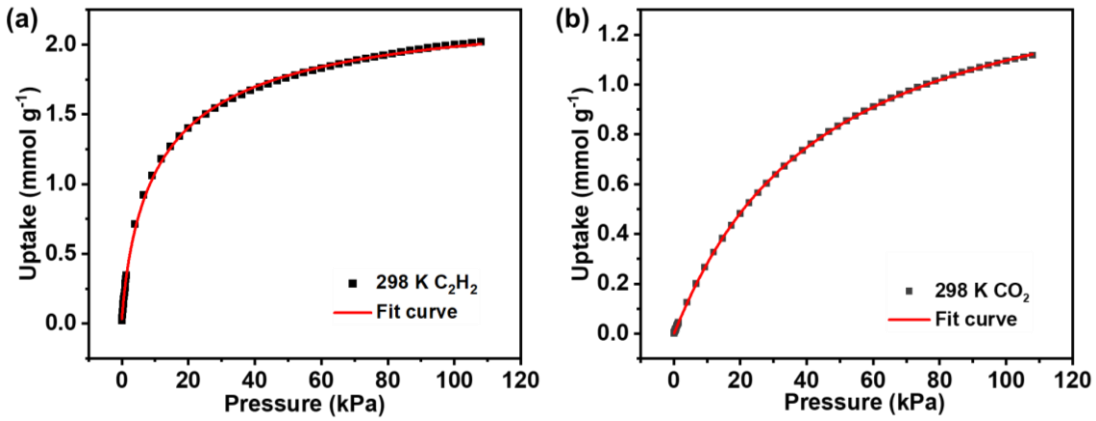

Fig. S9 (a) C_2H_2 and (b) CO_2 adsorption isotherms of In-TATB with fitting by the L–F model. Fitting results were given in Table S4.

Calculation of sorption heat by using Virial II model

$$\ln(P) = \ln(N) + \frac{1}{T}\sum_{i=0}^{m} a_i N^i + \sum_{j=0}^{n} b_j N^j \quad Q_{st} = -R\sum_{i=0}^{m} a_i N^i$$

The above equation was applied to fit the combined gas isotherm data for In-TATB at 273 and 298 K, where P is the pressure, N is the adsorbed amount, T is the temperature, a_i and b_i are virial coefficients, and m and n are the number of coefficients used to describe the isotherms. Q_{st} is the coverage-dependent enthalpy of adsorption and R is the universal gas constant.

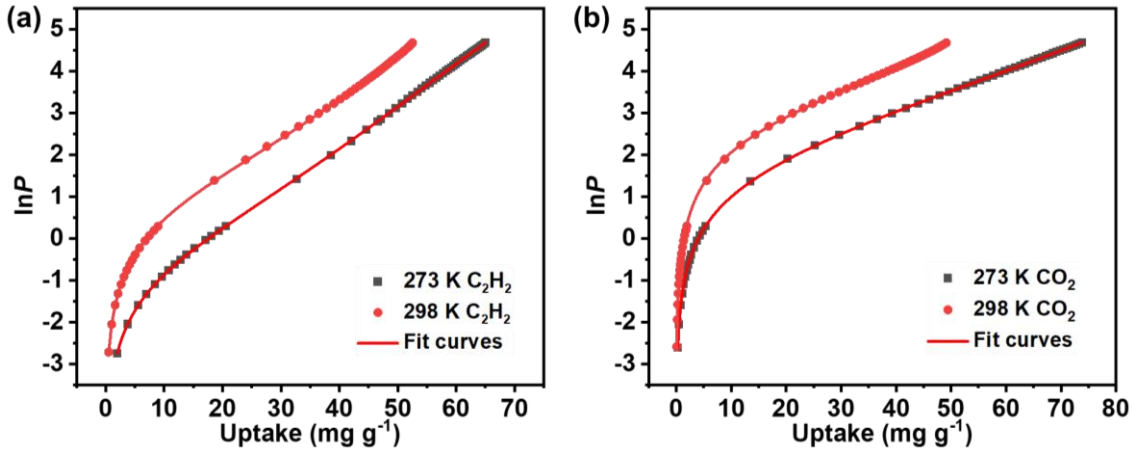

Fig. S10 Fitted adsorption isotherms for In-TATB with fitting by Virial II model. Fitting results were given in Table S5.

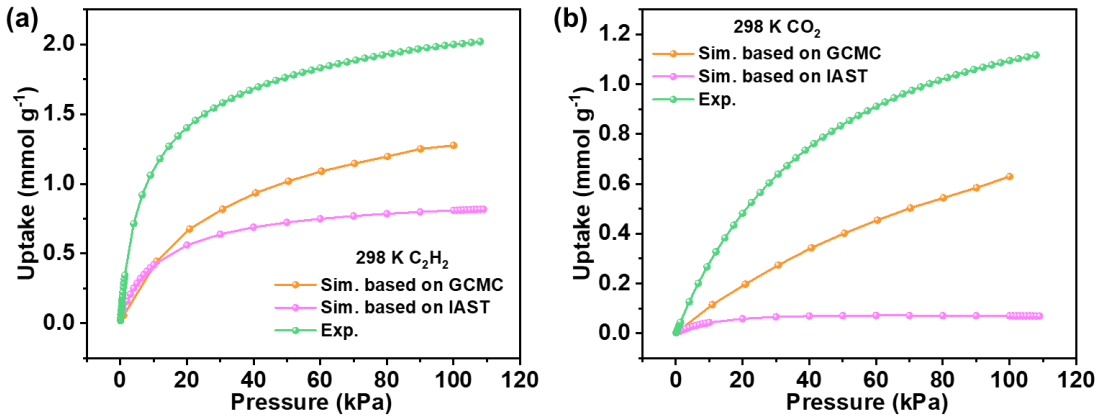

Fig. S11 Experimental and simulated adsorption isotherms of (a) C_2H_2 and (b) CO_2 at 298 K (0–1 bar).

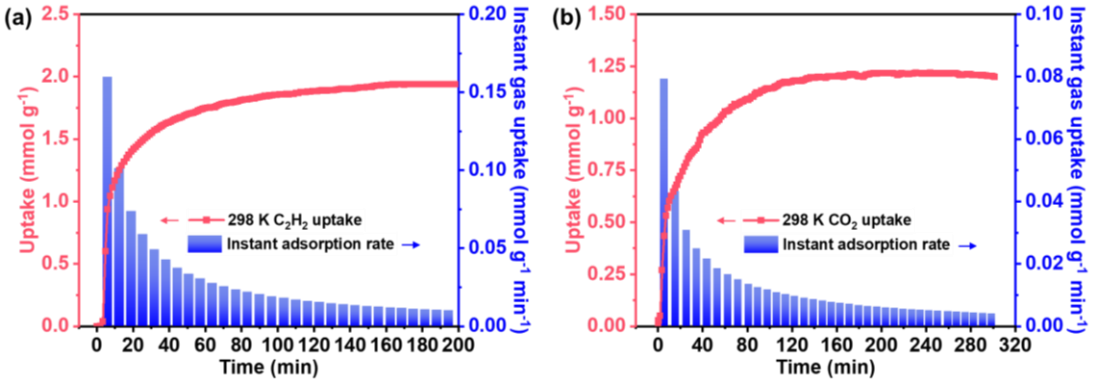

Fig. S12 Kinetic adsorption profiles and instant adsorption rates of (a) C_2H_2 and (b) CO_2 for In-TATB at 298 K and 1 bar.

Breakthrough experiments

The breakthrough experiment was performed on the BSD-MAB Multicomponent Adsorption Breakthrough Curve Analyzer at 298 K and 1 bar. A stainless steel column with a length of 70 mm and an inner diameter of 6 mm was used for sample packing. Activated crystalline sample (~1.2 g) was packed into the column. The column is placed in a circulating jacket connected to the thermostatic bath to control the temperature. Pressure control valve and mass flow controller are used to control the flow and pressure of the gas mixture. Outlet effluent from the column was continuously monitored using gas analytical mass spectrometer. The column packed with sample was firstly activated with N_2 flow of 10 mL min^{-1} for 8 h at 433 K. Between two breakthrough experiments, the adsorbent was regenerated by N_2 flow of 10 mL min^{-1} for 30 min at 393 K to guarantee complete removal of the adsorbed gases.

On the basis of the mass balance, the gas adsorption capacities can be determined as follows:

$$Q_i = \frac{C_i V}{22.4 \times m} \times \int_0^t (1 - \frac{F}{F_0}) dt$$

Where Q_i is the equilibrium adsorption capacity of gas i (mmol g^{-1}), C_i is the feed gas concentration, V is the volumetric feed flow rate (mL min^{-1}), t is the adsorption time (min), F_0 and F are the inlet and outlet gas molar flow rates, respectively, and m is the mass of the adsorbent (g).

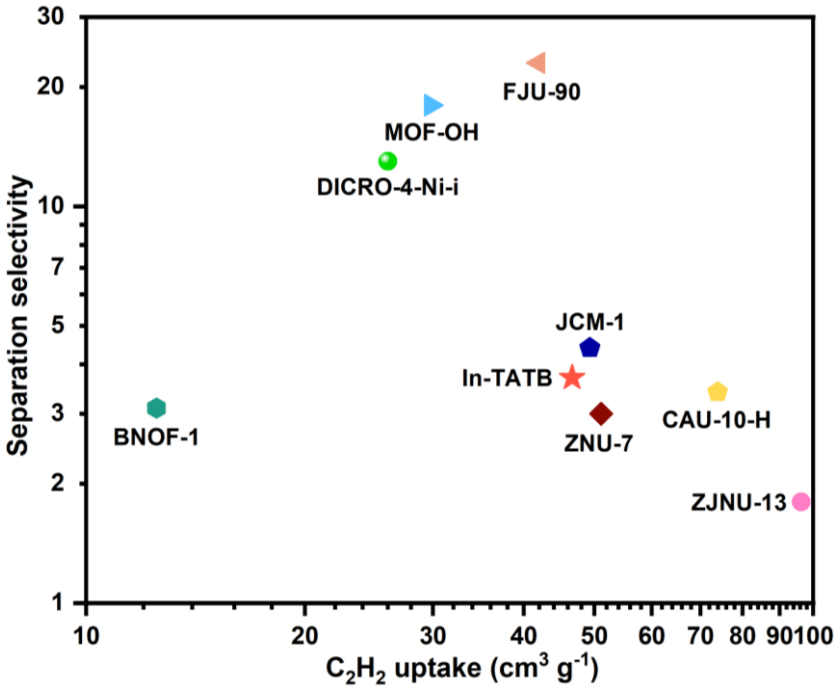

Fig. S13 Comparison of In-TATB with the reported materials for dynamic C_2H_2/CO_2 (50/50, *v*/*v*) separation at 298 K, except C_2H_2/CO_2/He = 10/5/85 for DICRO-4-Ni-i and C_2H_2/CO_2/Ar = 5/5/90 for BNOF-1.

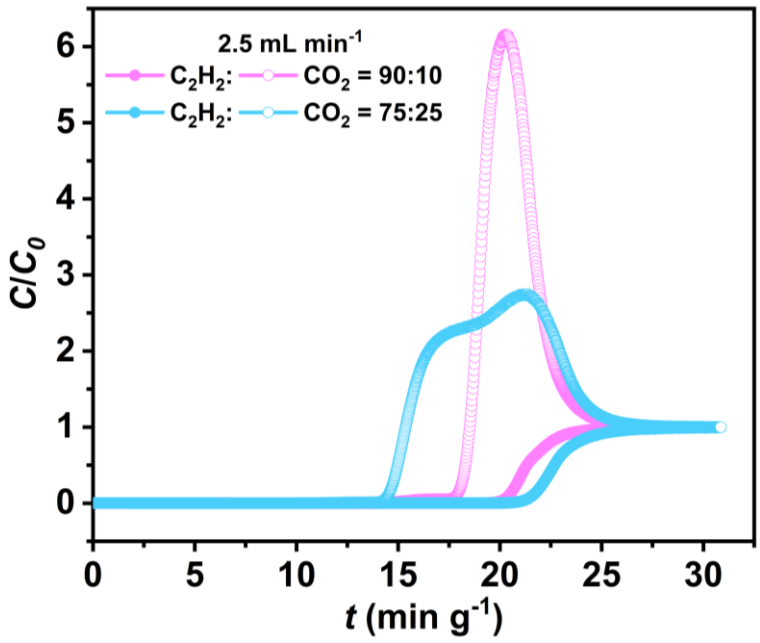

Fig. S14 Breakthrough plots for the separation of different C_2H_2/CO_2 mixtures on In-TATB at 298 K and 1 bar.

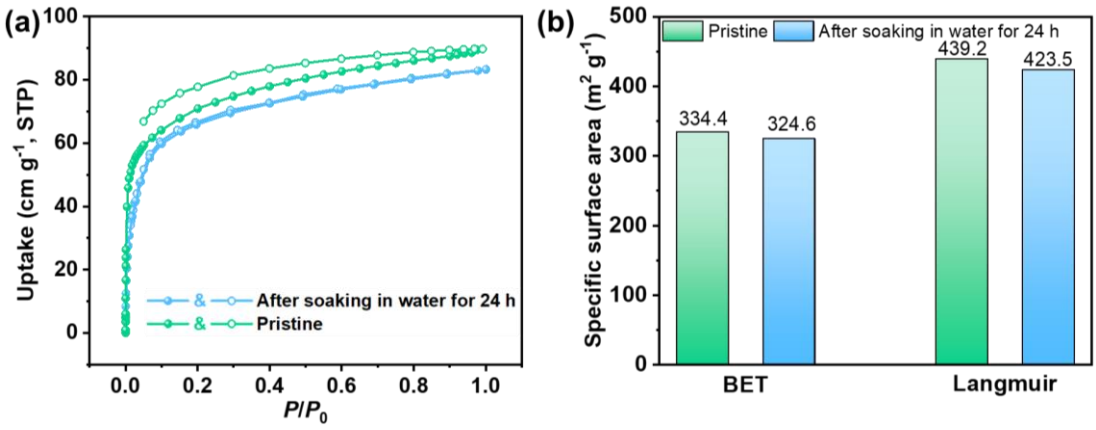

Fig. S15 Comparison of (a) CO_2 adsorption isotherms at 195 K and (b) BET/Langmuir surface areas of In-TATB.

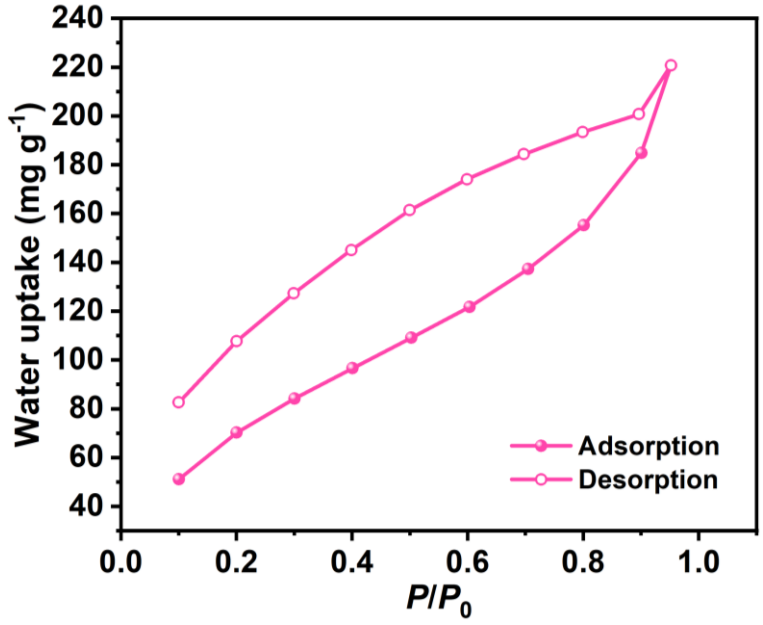

Fig. S16 Water vapor sorption isotherms of In-TATB at 298 K.

Table S1. Comparison of the adsorption capacity and Q_{st} of C_2H_2 and CO_2 and C_2H_2/CO_2 selectivity in In-TATB with some top-performing C_2H_2/CO_2 separation materials.

MOFs	C_2H_2 uptakes (cm g^{-1}) [a]	CO_2 uptakes (cm g^{-1}) [a]	C_2H_2 Q_{st} (kJ mol^{-1}) [b]	CO_2 Q_{st} (kJ mol^{-1}) [b]	C_2H_2/CO_2 selectivity[c]	Ref.
In-TATB	56.0	45.3	36.6	29.6	11.8	This work
TIFSIX-2-Cu-i	91.8	96.3	46.3	35.8	6.5[d]	(5)
BSF-1	52.6	39.6	30.7	21.7	3.4	(6)
TCuI	~48	~36	38.4	26.8	5.3	(7)
UTSA-220	76.2	75.7	29	27	4.4	(8)
SNNU-45	134.0	97	39.9	27.1	4.5	(9)
FeNi-M'MOF	96.1	60.9	27	24.5	24	(10)
DZU-1	90.6	67.9	31.7	30.6	6.1	(11)
MOF-OH	60	31.4	17.5	20.6	25	(12)
JCM-1	76.6	38.1	36.9	33.4	13.7	(13)
FJU-90	180	103	25.1	20.7	4.3	(14)
JNU-1	27.4	4.1	13.0	23.8	6.6	(15)
NUM-15	78.0	69.05	37.4	33.2	2.8	(16)
$CuZn_3(PDDA)_3(OH)$	104	48	28.9	24.1	3.3	(17)
MUF-17	67.4	56.2	49.5[e]	33.8[e]	6.01[e]	(18)
CAU-10-H	89.8[f]	60.0[f]	27[f]	25[f]	4[f]	(19)
ZNU-7	92.1	36.0	35.3	22.5	6.4	(20)
UTSA-74	103.5	67.9	31	25	9	(21)
JXNU-12 (F)	115.5	33.4	28.0	19.7	4.1	(22)
DICRO-4-Ni-i	43	23	37.7	33.9	13.9	(23)

[a] 298 K, 1 bar

[b] 298 K, 1 bar, at zero coverage

[c] 298 K, 1 bar, $C_2H_2 : CO_2 = 1 : 1$.

[d] $C_2H_2 : CO_2 = 2 : 1$.

[e] 293 K.

[f] 296 K

Table S2. Comparison of the C_2H_2/CO_2 (50/50, *v*/*v*) breakthrough performance of In-TATB with other materials at room temperature.

Adsorbent	Flow rate (mL min^{-1})	C_2H_2 uptakes (cm g^{-1})	Purity of C_2H_2 (%)	Breakthrough interval (min g^{-1})	Separation selectivity	Ref.
In-TATB	2.5	46.6	≥99.5	16.9	3.7	This work
SNNU-45	2.0	-	-	79.0	2.9	(9)
FeNi-M'MOF	2.0	4.1[a]	-	16	1.7	(10)
DZU-1	1.4	-	-	52.1	-	(11)
MOF-OH	2.0	29.8	-	~18	25	(12)
JCM-1	7.0	49.3	-	38.1	4.4	(13)
FJU-90	2.0	41.9	-	~23	-	(14)
JNU-1	2.0	63.6	-	75	-	(15)
NUM-15	2.0	-	-	8.4	-	(16)
$CuZn_3(PDDA)_3(OH)$	5.0	17.1	-	3.8	-	(17)
CAU-10-H	2.0	73.9	-	45	3.4	(19)
ZNU-7	2.5	51.1	-	-	3.0	(20)
DICRO-4-Ni-i	2.0[b]	26[b]	98.9	12[b]	13[b]	(23)
BNOF-1	5.0[c]	12.5[c]	-	25.3[c]	3.1[c]	(24)
ZJNU-13	2.0	96.3	81.2	58	1.8	(25)
ZNU-9	2.0	114.9	>99.3	45	-	(26)

[a] mol L^{-1}

[b] $C_2H_2/CO_2/He$ = 10/5/85

[c] $C_2H_2/CO_2/Ar$ = 5/5/90

X-ray crystallography

Diffraction data were collected at 199 K with a Mo Kα radiation (λ = 0.71073 Å) on a BrukerAXS SMART CCD area detector diffractometer. Absorption corrections were carried out utilizing SADABS routine. The structure was solved by the direct methods and refined using the SHELXTL program package. All non-hydrogen atoms were refined anisotropically with the hydrogen atoms added to their geometrically ideal positions and refined isotropically. The contribution of the disordered solvent molecules in the structure was subtracted from the reflection data by the SQUEEZE method as implemented in PLATON program. The final formula of In-TATB was determined by combining the single-crystal structures and TGA data. Data collection, structure refinement parameters for In-TATB (CCDC 2303160) are given in Table S3.

Table S3. The crystallographic data of In-TATB.

Name	In-TATB
Empirical formula	$C_{60}H_{48}In_3N_9O_{21}$
Formula weight	1575.53
Temperature/K	199.00
Crystal system	monoclinic
Space group	$P2_1/c$
a/Å	13.4568(10)
b/Å	31.007(3)
c/Å	18.5528(17)
α/°	90
β/°	105.270(2)
γ/°	90
Volume/Å^3	7467.8(11)
Z	4
D_{calc} (g cm^{-3})	1.401
F (000)	3144.0
Radiation	Mo Kα (λ = 0.71073)
Reflections collected	13145
R_{sigma}	0.0730
Goodness-of-fit on F^2	2.739
R_1,[a] wR_2[b] [$I \geq 2\sigma(I)$]	0.1503, 0.3623
R_1,[a] wR_2[b] [all data]	0.2029, 0.3978

[a]$R_1 = \Sigma||F_o| - |Fc||/\Sigma|F_o|$. [b]$wR_2 = [\Sigma w(F_o^2 - F_c^2)^2/\Sigma w(F_o^2)^2]^{1/2}$.

Table S4. Fitting results of CO_2 and C_2H_2 adsorption isotherms by L–F model.

	CO_2	C_2H_2
a_1	1.55752	2.34892
b_1	0.02043	0.132
c_1	1.03312	0.80855
Chi^2	3.76191E-6	2.10886E-4
R^2	0.99998	0.99963

Table S5. The fitting results of gas adsorption isotherms of In-TATB by Virial II model.

	CO_2	C_2H_2
b_0	11.59697	12.65099
b_1	-0.00841	0.02016
b_2	-0.00177	-0.00319
b_3	5.60778E-5	6.44932E-5
a_0	-3558.53364	-4403.63888
a_1	4.84655	1.82572
a_2	0.59128	0.95757
a_3	-0.0166	-0.01504
a_4	8.06551E-6	-2.54701E-5
Chi^2	2.25034E-4	2.13689E-4
R^2	0.99996	0.99996

References

1 A. K. Rappe and W. A. Goddard, *J. Phys. Chem.*, 2002, **95**, 3358−3363.

2 H. Cheng, Q. Wang, L. Meng, P. Sheng, Z. Zhang, M. Ding, Y. Gao and J. Bai, *ACS Appl. Mater. Interfaces*, 2021, **13**, 40713−40723.

3 W. L. Jorgensen, D. S. Maxwell and J. Tirado-Rives, *J. Am. Chem. Soc.*, 1996, **118**, 11225−11236.

4 J. J. Potoff and J. I. Siepmann, *AIChE J.*, 2001, **47**, 1676−1682.

5 K.-J. Chen, Hayley S. Scott, David G. Madden, T. Pham, A. Kumar, A. Bajpai, M. Lusi, Katherine A. Forrest, B. Space, John J. Perry and Michael J. Zaworotko, *Chem*, 2016, **1**, 753−765.

6 Y. Zhang, J. Hu, R. Krishna, L. Wang, L. Yang, X. Cui, S. Duttwyler and H. Xing, *Angew. Chem., Int. Ed.*, 2020, **59**, 17664−17669.

7 S. Mukherjee, Y. He, D. Franz, S.-Q. Wang, W.-R. Xian, A. A. Bezrukov, B. Space, Z. Xu, J. He and M. J. Zaworotko, *Chem.–Eur. J.*, 2020, **26**, 4923−4929.

8 H. Li, L. Li, R.-B. Lin, G. Ramirez, W. Zhou, R. Krishna, Z. Zhang, S. Xiang and B. Chen, *ACS Sustain. Chem. Eng.*, 2019, **7**, 4897−4902.

9 Y.-P. Li, Y. Wang, Y.-Y. Xue, H.-P. Li, Q.-G. Zhai, S.-N. Li, Y.-C. Jiang, M.-C. Hu and X. Bu, *Angew. Chem., Int. Ed.*, 2019, **58**, 13590−13595.

10 J. Gao, X. Qian, R.-B. Lin, R. Krishna, H. Wu, W. Zhou and B. Chen, *Angew. Chem., Int. Ed.*, 2020, **59**, 4396−4400.

11 B.-Y. Zhu, T. Zhang, C.-H. Li, J.-W. Cao, Z.-Q. Zhang, W. Qi, G.-Y. Wang, Z.-H. Rong, Y. Wang and K.-J. Chen, *Inorg. Chem.*, 2022, **61**, 4555−4560.

12 W. Gong, H. Cui, Y. Xie, Y. Li, X. Tang, Y. Liu, Y. Cui and B. Chen, *J. Am. Chem. Soc.*, 2021, **143**, 14869−14876.

13 J. Lee, C. Y. Chuah, J. Kim, Y. Kim, N. Ko, Y. Seo, K. Kim, T. H. Bae and E. Lee, *Angew. Chem., Int. Ed.*, 2018, **57**, 7869−7873.

14 Y. Ye, Z. Ma, R.-B. Lin, R. Krishna, W. Zhou, Q. Lin, Z. Zhang, S. Xiang and B. Chen, *J. Am. Chem. Soc.*, 2019, **141**, 4130−4136.

15 H. Zeng, M. Xie, Y.-L. Huang, Y. Zhao, X.-J. Xie, J.-P. Bai, M.-Y. Wan, R. Krishna,

W. Lu and D. Li, *Angew. Chem., Int. Ed.*, 2019, **58**, 8515−8519.

16 Q. Zhang, L. Zhou, P. Liu, L. Li, S.-Q. Yang, Z.-F. Li and T.-L. Hu, *Sep. Purif. Technol.*, 2022, **296**, 121404.

17 B. Zhang, Y. Rao, L. Hou, B. Liu and Q. Li, *ACS Materials Lett.*, 2022, **4**, 1774−1779.

18 O. T. Qazvini, R. Babarao and S. G. Telfer, *Chem. Mater.*, 2019, **31**, 4919−4926.

19 J. Pei, H.-M. Wen, X.-W. Gu, Q.-L. Qian, Y. Yang, Y. Cui, B. Li, B. Chen and G. Qian, *Angew. Chem., Int. Ed.*, 2021, **60**, 25068−25074.

20 N. Xu, T. Yan, J. Li, L. Wang, D. Liu and Y. Zhang, *Inorg. Chem. Front.*, 2023, **10**, 522−528.

21 F. Luo, C. Yan, L. Dang, R. Krishna, W. Zhou, H. Wu, X. Dong, Y. Han, T. L. Hu, M. O'Keeffe, L. Wang, M. Luo, R.-B. Lin and B. Chen, *J. Am. Chem. Soc.*, 2016, **138**, 5678−5684.

22 X.-P. Fu, Y.-L. Wang, X.-F. Zhang, R. Krishna, C.-T. He, Q.-Y. Liu, Y.-L. Wan and B. Chen, *Chem. Eng. J.*, 2022, **432**, 134433.

23 H. S. Scott, M. Shivanna, A. Bajpai, D. G. Madden, K.-J. Chen, T. Pham, K. A. Forrest, A. Hogan, B. Space, J. J. Perry IV and M. J. Zaworotko, *ACS Appl. Mater. Interfaces*, 2017, **9**, 33395−33400.

24 W. Wang, L. Wang, F. Du, G.-D. Wang, L. Hou, Z. Zhu, B. Liu and Y.-Y. Wang, *Chem. Sci.*, 2023, **14**, 533−539.

25 T. Xu, Z. Jiang, P. Liu, H. Chen, X. Lan, D. Chen, L. Li and Y. He, *ACS Appl. Nano Mater.*, 2020, **3**, 2911−2919.

26 Y. Zhang, W. Sun, B. Luan, J. Li, D. Luo, Y. Jiang, L. Wang and B. Chen, *Angew. Chem., Int. Ed.*, 2023, **62**, e202309925.